

Quantum Monte Carlo simulation of spin-polarized H

L. Vranješ Markić

*Faculty of Natural Sciences, University of Split, 21000 Split, Croatia
Institut für Theoretische Physik, Johannes Kepler Universität, A 4040 Linz, Austria*

J. Boronat and J. Casulleras

*Departament de Física i Enginyeria Nuclear, Campus Nord B4-B5,
Universitat Politècnica de Catalunya, E-08034 Barcelona, Spain*

(Dated: January 28, 2017)

The ground-state properties of spin polarized hydrogen $H\downarrow$ are obtained by means of diffusion Monte Carlo calculations. Using the most accurate to date ab initio $H\downarrow$ - $H\downarrow$ interatomic potential we have studied its gas phase, from the very dilute regime until densities above its freezing point. At very small densities, the equation of state of the gas is very well described in terms of the gas parameter ρa^3 , with a the s-wave scattering length. The solid phase has also been studied up to high pressures. The gas-solid phase transition occurs at a pressure of 173 bar, a much higher value than suggested by previous approximate descriptions.

PACS numbers: 67.65.+z, 02.70.Ss

I. INTRODUCTION

The suggestion of Stwalley and Nosanow¹ in 1976 that electron-spin-polarized gases of hydrogen ($H\downarrow$) could be an ideal candidate for achieving a Bose-Einstein condensate (BEC) state opened an intense experimental search which finally led to its first observation in Rb, Na and Li in 1995.² The success attained in cold alkali gases was made possible due to techniques like evaporative cooling developed previously for confining $H\downarrow$. The realization of a BEC state of hydrogen was finally achieved in 1998 by Fried *et al.*³ after overcoming arduous problems like recombination on the walls, by working with a wall-free confinement, and low evaporation rates by using spin resonance. Also in 1998, Safonov *et al.*⁴ observed a quasi-condensate in two-dimensional (2D) $H\downarrow$ adsorbed on liquid ⁴He. This is one of the best realizations of a 2D quantum system since the adsorption energy of $H\downarrow$ on ⁴He is only ~ 1 K and the adsorbed gas floats approximately 8 Å apart from the liquid. Further experimental work is still necessary to observe in this system signals of the Berezinskii-Kosterlitz-Thouless transition, which has been recently observed in a trapped gas of Rb confined in such a way that atoms can move only within a plane.⁵

Hydrogen is the simplest element and its main properties are well known theoretically, starting from the interatomic interaction which can be computed almost exactly.⁶ This is significantly different from alkali gases in which the interaction is much more involved and, in general, less well known. Its s-wave scattering length a is appreciably smaller than the typical values for alkalis, a feature that retards evaporative cooling and produces a higher transition temperature (50 μ K). Spin-polarized hydrogen atoms interact via the triplet potential $b^3\Sigma_u^+$ determined in an essentially exact way by Kolos and Wolniewicz,⁶ and recently extended to larger interparticle distances by Jamieson *et al.*⁷ The $H\downarrow$ - $H\downarrow$ interaction is

highly repulsive at short distances and presents a shallow minimum of ~ 6 K at $r \sim 4\text{Å}$. The combination of this extremely weak attraction and its light mass explains why $H\downarrow$ remains in the gas phase even in the limit of zero temperature. A measure of the quantum character of a given system can be drawn through the quantum parameter,⁸

$$\eta = \frac{\hbar^2}{m\epsilon\sigma^2}, \quad (1)$$

with ϵ and σ the well depth and core of the interaction, respectively. According to this definition, $\eta = 0.5$ for $H\downarrow$ which is the highest value for η among all the quantum fluids (for instance, $\eta = 0.2$ for ⁴He).

From a theoretical viewpoint, bulk $H\downarrow$ was first studied by Ethers *et al.*⁹ using the variational Monte Carlo (VMC) method and by Miller and Nosanow⁸ using integral equations for computing the multidimensional integrals of the variational approach. Both calculations showed that the ground state of $H\downarrow$ is unbound at any pressure. Lantto and Nieminen¹⁰ confirmed this result using the Euler-Lagrange hypernetted chain equation and estimated values for the condensate fraction of the gas at different densities for the first time. More recently, Entel and Anlauf¹¹ carried out a new VMC calculation of properties of the gas phase such as the energy, condensate fraction and excitation spectrum. The heavier isotopes spin-polarized deuterium $D\downarrow$ and tritium $T\downarrow$ have also been studied theoretically. $D\downarrow$ atoms obey Fermi statistics and their three versions, involving one ($D\downarrow_1$), two ($D\downarrow_2$) and three ($D\downarrow_3$) equally occupied nuclear spin states, were analyzed by Panoff and Clark¹² and Flynn *et al.*¹³ using both VMC and Fermi-hypernetted chain theory (FHNC). From the results obtained, they concluded that $D\downarrow_2$ and $D\downarrow_3$ are both liquids at zero pressure. Their conclusion has been confirmed by Skjetne and Østgaard¹⁴, using a lowest-order constrained variational method. On the other hand, microscopic properties of bosonic tritium $T\downarrow$ clusters have been recently studied by

Blume *et al.*¹⁵ using the diffusion Monte Carlo (DMC) method, and their results suggest the use of T \downarrow as a new BEC gas with the advantage of a nearly exact knowledge of the interatomic potential.

In the present work, we present a DMC study of the gas and solid phases of spin-polarized hydrogen. Using recent updates of the *ab initio* H \downarrow -H \downarrow interatomic potential and relying on the accuracy of the DMC method, we report accurate microscopic results for energetic and structural properties of the bulk system. In the very low density regime, the energy is well reproduced by the well-known analytical expansion in terms of the gas parameter ρa^3 ,^{16,17,18} with a the s-wave scattering length obtained by solving the two-body Schrödinger equation with the chosen interatomic potential. A relevant result of our work is an accurate computation of the gas-solid phase transition point which is predicted to occur at pressures significantly higher than previous predictions based on quantum theory of corresponding states¹ and VMC simulations.¹⁹

In Sec. II, we report briefly the DMC method and discuss the trial wave functions used for importance sampling in the gas and solid phases. In Sec. III, the results of the DMC simulations are reported in several subsections. In the first one, we review the H \downarrow -H \downarrow interatomic potentials and compare our results at the variational level with some previous estimations. The second and third parts are devoted to the microscopic results for the gas and solid phases, respectively. In the last one, we study the gas-solid phase transition point and report results on the freezing and melting densities. Finally, Sec. IV comprises a summary of the work and an account of the main conclusions.

II. METHOD

The DMC method is nowadays a well-known tool devised to study quantum fluids and solids at zero temperature. Its starting point is the Schrödinger equation written in imaginary time,

$$-\hbar \frac{\partial \Psi(\mathbf{R}, t)}{\partial t} = (H - E_r) \Psi(\mathbf{R}, t), \quad (2)$$

with an N -particle Hamiltonian

$$H = -\frac{\hbar^2}{2m} \sum_{i=1}^N \nabla_i^2 + \sum_{i<j}^N V(r_{ij}). \quad (3)$$

In Eq. (2), E_r is a constant acting as a reference energy and $\mathbf{R} \equiv (\mathbf{r}_1, \dots, \mathbf{r}_N)$ is a *walker* in Monte Carlo terminology.

DMC solves stochastically the Schrödinger equation (2) replacing $\Psi(\mathbf{R}, t)$ by $\Phi(\mathbf{R}, t) = \Psi(\mathbf{R}, t)\psi(\mathbf{R})$, with $\psi(\mathbf{R})$ a trial wave function used for importance sampling.

In this way equation (2) becomes

$$-\frac{\partial \Phi(\mathbf{R}, t)}{\partial t} = -D \nabla_{\mathbf{R}}^2 \Phi(\mathbf{R}, t) + D \nabla_{\mathbf{R}} \cdot (\mathbf{F}(\mathbf{R}) \Phi(\mathbf{R}, t)) + (E_L(\mathbf{R}) - E) \Phi(\mathbf{R}, t), \quad (4)$$

where $D = \hbar^2/(2m)$, $E_L(\mathbf{R}) = \psi(\mathbf{R})^{-1} H \psi(\mathbf{R})$ is the local energy, and

$$\mathbf{F}(\mathbf{R}) = 2 \psi(\mathbf{R})^{-1} \nabla_{\mathbf{R}} \psi(\mathbf{R}) \quad (5)$$

is the drift force which guides the diffusion process. In Eq. (4), when $t \rightarrow \infty$ only the lowest energy eigenfunction, not orthogonal to $\psi(\mathbf{R})$, survives and then the sampling of the ground state is effectively achieved. Apart from statistical uncertainties, the energy of a N -body bosonic system is exactly calculated.

The trial wave function used for the simulation of the gas phase is of Jastrow form, $\psi_J(\mathbf{R}) = \prod_{i<j}^N f(r_{ij})$, with a two-body correlation function $f(r)$ of the form

$$f(r) = \exp[-b_1 \exp(-b_2 r)], \quad (6)$$

where b_1 and b_2 are variational parameters. This form has been taken from the VMC work of Eters *et al.*,⁹ who used a Morse potential fitted to reproduce Kolos and Wolniewicz *ab initio* data.⁶ It corresponds to the WKB solution of the two-body Schrödinger equation for small interparticle distances when the potential is of Morse type.

Simulations of the crystalline bcc, fcc and hcp phases have been also carried out; in this case, we use a Nosanow-Jastrow model

$$\psi_{\text{NJ}}(\mathbf{R}) = \psi_J(\mathbf{R}) \prod_i^N g(r_{iI}), \quad (7)$$

where $g(r) = \exp(-\alpha r^2/2)$ is a localizing function which links every particle i to a point \mathbf{r}_I of the lattice. The parameter α is optimized variationally.

The variational parameters b_1 , b_2 , and α (6,7) have been obtained at different densities by optimizing the variational energy calculated with the VMC method. For example, in the gas phase and at a density $\rho = 0.0079 \text{ \AA}^{-3}$ the values are $b_1 = 82$ and $b_2 = 1.32 \text{ \AA}^{-1}$; b_1 increases with density whereas b_2 remains practically constant. In the solid phase the most relevant parameter is α , which increases from a value 0.3 \AA^{-2} at melting density up to 1.3 \AA^{-2} at the highest density here studied; the Jastrow parameters are kept fixed in all the solid density range, $b_1 = 70$ and $b_2 = 1.32 \text{ \AA}^{-1}$. The statistical errors of the variational energies are similar to those of the DMC results (see Tables I and II).

We use the DMC method accurate to second order in the time step Δt ,²⁰ and then larger Δt values than in linear DMC algorithms can be used. We have studied both the time-step and the mean walker population in order to eliminate any bias coming from them. Finally, we have analyzed carefully the size dependence of our simulations. The calculations on the gas phase have been

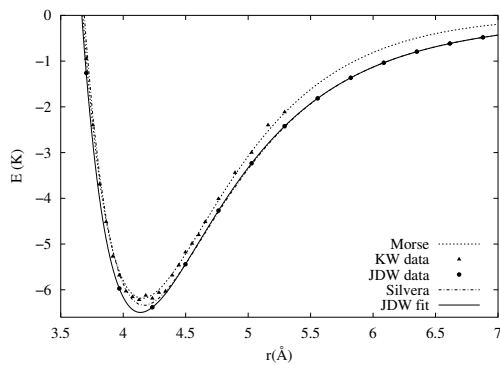


FIG. 1: $H\downarrow$ - $H\downarrow$ interatomic potentials.

carried out with 128 atoms and some checks with 150 and 170 atoms have also been made. Using standard tail corrections, which assume a uniform system ($g(r) = 1$) beyond $r > L/2$, with L the length of the simulation box, the size dependence of the energy remains smaller than the typical size of the statistical errors. The size effects are larger in the calculations of the solid phase. In this case, we have used 128, 108, and 180 atoms for the bcc, fcc, and hcp lattices. To consider tail corrections in the same form as in the gas phase is a rough approximation due to the periodic order of the solid. In order to overcome this difficulty, we have studied the size dependence of the energy at the VMC level where larger number of particles can be used. From the VMC results one extracts the tail corrections for a given number of atoms and then these are added to the DMC energies. It has been verified²¹ that this procedure is able to reproduce accurately the experimental equation of state of solid ^4He .

III. RESULTS

A. Interatomic potential

Spin-polarized hydrogen atoms interact via the triplet potential $b\ ^3\Sigma_u^+$, calculated with high precision by Kolos and Wolniewicz (KW) in 1965.⁶ Due to the simplicity of the H atom it is possible to calculate this potential in an essentially exact way. More recently, it has been recalculated up to larger interatomic distances by Jamieson, Dalgarno and Wolniewicz (JDW).⁷ The differences between the KW and JDW potentials, in the range where they can be compared, are rather small, as shown in Fig. 1. The addition of mass-dependent adiabatic corrections, which have been calculated by Kolos and Rychlewski,²² to JDW potential, can not be discerned in Fig. 1.

In the past, only the KW potential has been used in the study of the $H\downarrow$ gas. Usually, an analytic form was assumed and then the free parameters of the model were fitted to reproduce the KW data. In this way, Etters *et al.*⁹ used a Morse potential whereas Silvera and Goldman²³ proposed a form which is similar to the ones used

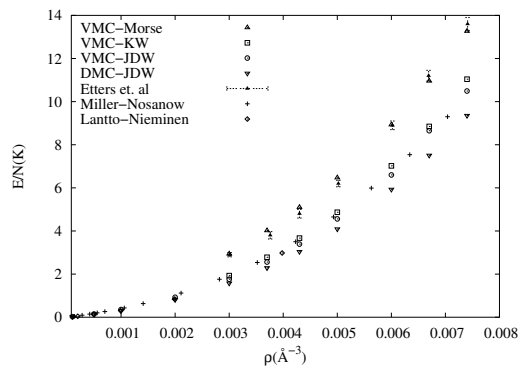


FIG. 2: Influence of the interatomic potential on the equation of state of gas $H\downarrow$.

for He-He potentials. The results of these models are also plotted in Fig. 1. In the present work, we have used the JDW interaction and a cubic spline to interpolate between the reported points. The resulting potential is plotted as a solid line in Fig. 1. The JDW data are smoothly connected with the long-range behavior of the H-H potential as calculated by Yan *et al.*²⁴ The JDW potential has a core diameter of 3.67 Å and a minimum $\epsilon = -6.49$ K (slightly deeper than KW) at a distance $r_m = 4.14$ Å.

The influence of the potential on the energy of the gas at small densities is shown in Fig. 2. We have carried out VMC calculations using the trial wave function (6) introduced in the previous Section and the KW and JDW potentials. The JDW energies are below the KW ones in all the density range, reflecting the slightly deeper well of the JDW potential. If we use the Morse potential adjusted by Etters *et al.*⁹ to the KW data, the VMC energies are significantly worse with respect to the KW ones. This manifests the difficulties on fitting a functional form to the *ab initio* KW data; the Morse potential is a bit more repulsive than KW and therefore the energies are higher. As a matter of comparison, we also show in Fig. 2 results from previous calculations. The results from Etters *et al.*⁹ using the Morse potential are in nice agreement with our VMC results using the same potential. The variational results of Miller and Nosanow⁸ used the KW data and are in close agreement with our present VMC results with the same interaction. Finally, results of Lantto and Nieminen¹⁰ are also reported; they used the KW potential and performed an Euler-Lagrange-HNC calculation. Their results, restricted to very low densities, are slightly better than ours due to their use of an optimized Jastrow factor. All these variational results, both ours and from previous works, are compared in the same Figure with present DMC results with the JDW interaction. As expected, the DMC results are below the VMC ones in all the density range with a difference that increases with ρ , a predictable feature attending to the fact that the Jastrow factor (6) corresponds to an analytical form which approximates the wave function solution of the two-body

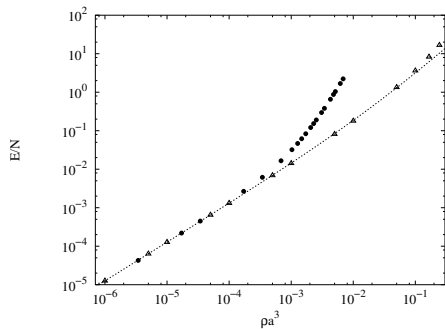


FIG. 3: Equation of state of gas $\text{H}\downarrow$ as a function of the gas parameter ρa^3 in units of $\hbar^2/(2ma^2)$ (solid points). The triangles correspond to a HS gas²⁵ and the line to Eq.(8).

problem.

B. Gas phase

The gas phase of spin-polarized H at very low densities is of special relevance for the field of Bose-condensed gases at low temperatures. The case of H is even more appealing than alkali gases from a theoretical perspective because the interatomic interaction between $\text{H}\downarrow$ atoms is very well known, as we have commented in the previous subsection. At sufficiently low densities, the equation of state becomes universal when it is written in terms of the gas parameter $x = \rho a^3$, with a the s-wave scattering length. The equation of state of a bosonic gas at low densities is given by

$$\left(\frac{E}{N}\right) = 4\pi x \left(1 + \frac{128}{15\sqrt{\pi}} x^{1/2}\right), \quad (8)$$

where the first term is the mean-field result,¹⁶ and the second is the Lee-Huang-Yang correction;¹⁷ the energy per particle is written in units of $\hbar^2/(2ma^2)$.

In Fig. 3, the energy per particle of gas $\text{H}\downarrow$ is compared to the universal equation of phase (8) and to DMC results for a hard-sphere (HS) gas from Ref. 25. In order to carry out this comparison we have calculated the s-wave scattering length of the JDW potential used in the present work. The value obtained, $a = 0.697 \text{ \AA}$ agrees with previous determinations.^{15,26} As one can see in the figure, the equation of state of gas $\text{H}\downarrow$ coincides with both the analytic law (8) and the HS results up to $x \simeq 10^{-4}$ in agreement with the range of universality determined in Ref. 25. Beyond this value, the energies of bulk $\text{H}\downarrow$ clearly separate from Eq. (8), increasing with x faster than for HS gas.

The condensate fraction n_0 , i.e., the fraction of particles occupying the zero momentum state, presents also a universal behavior in terms of the gas parameter x at very low densities. According to the Bogoliubov formula,¹⁶

$$n_0 = 1 - \frac{8}{3\sqrt{\pi}} x^{1/2}. \quad (9)$$

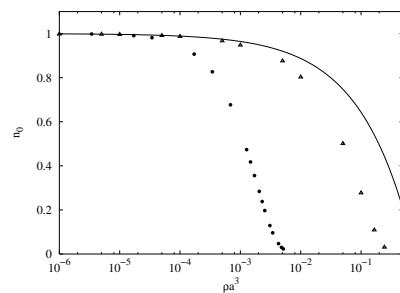


FIG. 4: Condensate fraction of gas $\text{H}\downarrow$ as a function of the gas parameter ρa^3 (solid points). The triangles correspond to a HS gas²⁵ and the line to the Bogoliubov approximation (9).

ρ (\AA^{-3})	E/N (K)	T/N (K)	P (bar)	c (m/s)
0.0001	0.0221(5)	0.101(1)	0.000321(3)	19.9(2)
0.001	0.302(3)	1.213(6)	0.0548(4)	90.8(6)
0.005	4.091(8)	9.55(3)	5.65(5)	470(4)
0.01	18.68(6)	27.40(13)	61.3(6)	1149(13)
0.0125	32.13(6)	38.61(2)	138.4(1.6)	$1.56(2) \times 10^3$
0.015	51.07(8)	51.9(3)	273(3)	$2.02(3) \times 10^3$
0.02	109.24(16)	83.2(5)	819(12)	$3.08(5) \times 10^3$

TABLE I: Results for gas $\text{H}\downarrow$ at different densities ρ : energy per particle (E/N), kinetic energy per particle (T/N), pressure (P), and speed of sound (c). Figures in parenthesis are the statistical errors.

The condensate fraction has been obtained from the long-range behavior of the one-body density matrix $\rho(r)$, $n_0 = \lim_{r \rightarrow \infty} \rho(r)$. We have verified by increasing the number of particles of the simulation at different densities that the size dependence of n_0 is smaller than its statistical error. In Fig. 4, we compare our results for the condensate fraction of gas $\text{H}\downarrow$ with Eq. (9). DMC results²⁵ for n_0 in the HS system are also plotted in the same figure. As one can see, the three results are coincident up to $x \simeq 10^{-4}$, the same value observed for the energy in Fig. 3. Both HS and $\text{H}\downarrow$ show a faster decrease with x than the law (9), the departure from it being significantly larger for hydrogen, in agreement with the same feature observed in Fig. 3 for the energy.

Spin-polarized H in its gas phase has been studied in all the density range up to densities above crystallization. DMC results for the total and kinetic energy per particle at different densities are reported in Table I. In order to remove any residual bias from the trial wave function, kinetic energies are calculated as differences between total energies and pure estimations of potential energies. The energies are positive everywhere, proving its gaseous nature, and dominated by the kinetic part which is larger than the potential energy (in absolute values) at any density. The potential energy per particle is negative up to a density $\rho = 0.015 \text{ \AA}^{-3}$, presenting a minimum value of -9 K at a density $\rho = 0.01 \text{ \AA}^{-3}$, and then becomes positive.

In Fig. 5, we plot the present DMC results for the

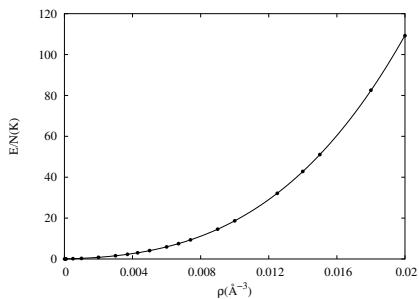


FIG. 5: Energy per particle of gas $H\downarrow$ (solid circles) as a function of the density ρ . The solid line corresponds to the fit to the DMC energies using Eq. (10). The error bars of the DMC energies are smaller than the size of the symbols.

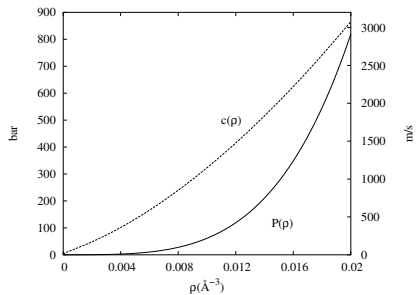


FIG. 6: Pressure and speed of sound of gas $H\downarrow$ as a function of the density. Left (right) scale corresponds to pressure (speed of sound).

equation of state of the gas. Our results are well parameterized by a polynomial form ($e \equiv E/N$)

$$e(\rho) = e_1\rho + e_2\rho^2 + e_3\rho^3 + e_4\rho^4, \quad (10)$$

shown as a solid line on top of the DMC results in Fig. 5. The best set of parameters is: $e_1 = 217.0(1.9) \text{ K}\text{\AA}$, $e_2 = 7.76(9) \times 10^4 \text{ K}\text{\AA}^2$, $e_3 = 8.23(12) \times 10^6 \text{ K}\text{\AA}^3$, and $e_4 = 5.1(5) \times 10^7 \text{ K}\text{\AA}^4$, the figures in parenthesis being the statistical uncertainties.

Using the equation of state (10), the pressure is easily derived from its thermodynamic definition

$$P(\rho) = \rho^2(\partial e / \partial \rho); \quad (11)$$

and from it, the corresponding speed of sound as a function of the density

$$c^2(\rho) = \frac{1}{m} \left(\frac{\partial P}{\partial \rho} \right). \quad (12)$$

Results for the pressure P and the speed of sound c for some values of the density, where specific DMC simulations have been carried out, are reported in Table I. The functions $P(\rho)$ and $c(\rho)$, derived respectively from Eqs. (11) and (12), are shown in Fig. 6.

DMC simulations allow also for exact estimations of other relevant magnitudes such as the two-body radial distribution function $g(r)$ and its Fourier transform, the

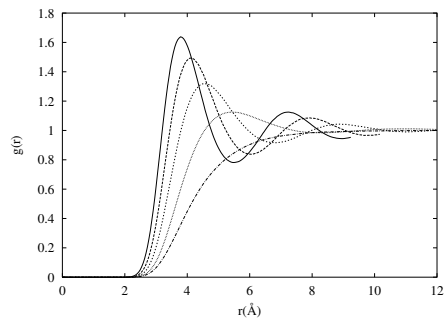


FIG. 7: Two-body radial distribution functions of the gas phase. From bottom to top in the height of the main peak, the results correspond to densities 0.002, 0.0067, 0.01, 0.0125, and 0.015 \AA^{-3} .

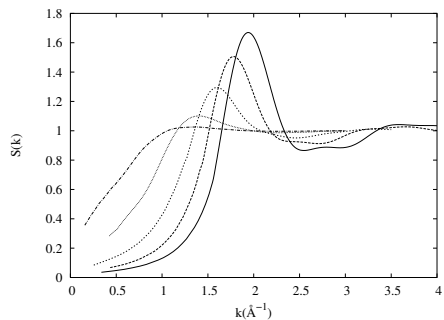


FIG. 8: Static structure function of the gas phase. From bottom to top in the height of the main peak, the results correspond to densities 0.002, 0.0067, 0.01, 0.0125, and 0.015 \AA^{-3} .

static structure function $S(k)$. With the use of pure estimators²⁷ it is possible to eliminate the bias coming from the trial wave function and arrive to exact results for both functions. The evolution of $g(r)$ with density for the gas $H\downarrow$ is shown in Fig. 7. At the smallest density reported, $g(r)$ is a monotonic function with the corresponding *hole* consequence of the repulsive core of the interatomic interaction. When ρ increases $g(r)$ gains structure, with the main peak that shifts to shorter distances and increases its strength.

In Fig. 8, results of $S(k)$ at the same densities as in Fig. 7 are reported. The results show the expected behavior: when ρ increases, the strength of the main peak increases and moves to higher momenta in a monotonic way. At low momenta, the slope of $S(k)$ decreases with the density, following the limiting behavior $\lim_{k \rightarrow 0} S(k) = \hbar k / (2mc)$ driven by the speed of sound c . As expected, the DMC data start at a finite k value inversely proportional to the box size L .

To end this subsection, we show in Fig. 9 the density dependence of the condensate fraction from the very dilute regime up to densities corresponding to freezing. The full set of data is well reproduced using the func-

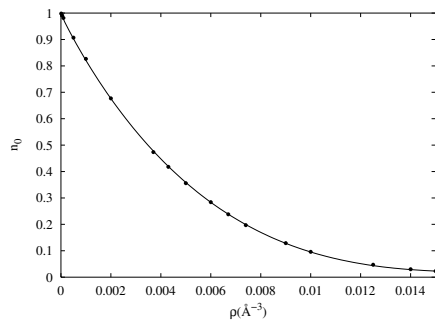


FIG. 9: Condensate fraction of spin-polarized H in the gas phase. The line corresponds to a fit to the DMC data using Eq.(13). The error bars are smaller than the size of the symbols.

tional form

$$n_0(\rho) = 1 - \frac{8}{3\sqrt{\pi}}(\rho a^3)^{1/2} - b_1 \rho a^3 - b_2 (\rho a^3)^2 - b_3 (\rho a^3)^{5/2}, \quad (13)$$

which is also plotted in the figure as a solid line on top of the DMC results. The values of the parameters in Eq. (13) are $b_1 = 504(5)$, $b_2 = -1.254(49) \times 10^5$, $b_3 = 8.54(55) \times 10^5$, and a is the scattering length.

C. Solid phase

The solid phase of spin-polarized H has been studied by using as importance sampling trial wave function a Nosanow-Jastrow model (7). The geometry of the lattice is defined by a proper selection of the lattice sites \mathbf{r}_I around which the atoms are organized according to a commensurate solid. There is no experimental measurement on solid H \downarrow at the pressures in which we are interested in and nothing is known about the form of its solid lattice at low temperatures. We have carried out calculations of the solid phase at some densities using the fcc, hcp, and bcc lattices. Near the melting density the bcc phase is slightly better and, at higher densities, the differences between them are not distinguishable within the statistical noise: at $\rho = 0.0125 \text{ \AA}^{-3}$, $E/N = 33.12(4)$, $34.30(5)$, and $33.02(8)$ K, and at $\rho = 0.018 \text{ \AA}^{-3}$, $E/N = 76.2(2)$, $76.2(2)$, and $76.1(2)$ K for fcc, hcp, and bcc respectively. Therefore, we decided to study the solid H \downarrow properties assuming a bcc phase. It is worth noticing that the same lattice was used in the past by Pierleoni *et al.*²⁸ in the study of solid H at very high pressure.

Some selected results for the total and kinetic energies per particle are reported in Table II. The behavior of the partial energies, potential and kinetic, is very similar to the one obtained for the gas: the kinetic energy dominates in all the density regime and the potential energy is negative at the lower densities and becomes positive for densities $\rho \geq 0.02 \text{ \AA}^{-3}$. The full set of results for the energy of the solid phase is shown in Fig. 10. The solid

ρ (\AA^{-3})	E/N (K)	T/N (K)	P (bar)	c (m/s)
0.0125	33.02(8)	43.4(1)	121.6(2)	1445(3)
0.015	49.38(8)	59.0(6)	236.4(5)	1866(4)
0.02	99.6(2)	93.1(6)	679.8(1.4)	2821(6)
0.0225	134.9(2)	107.8(6)	1096(2)	3350(7)
0.025	178.5(2)	123.7(7)	1648(3)	3909(8)

TABLE II: Results for solid H \downarrow at different densities ρ : energy per particle (E/N), kinetic energy per particle (T/N), pressure (P), and speed of sound (c). Figures in parenthesis are the statistical errors.

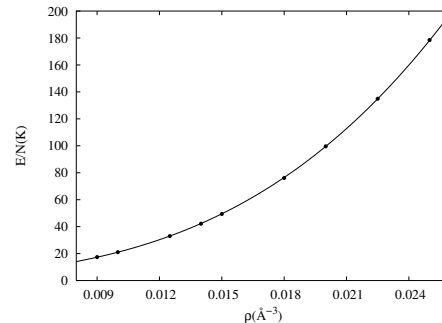


FIG. 10: Energy per particle of solid H \downarrow (solid circles) as a function of the density ρ . The solid line corresponds to the fit to the DMC energies using Eq. (14). The error bars of the DMC energies are smaller than the size of the symbols.

line on top of the DMC results correspond to a numerical fit obtained using the function

$$e(\rho) = s_1 \rho + s_3 \rho^3. \quad (14)$$

The optimal values in Eq. (14) are $s_1 = 1147(6) \text{ K\AA}$ and $s_3 = 9.57(2) \times 10^6 \text{ K\AA}^3$.

From the functional form (14), and using the corresponding thermodynamic expressions for the pressure (11) and the speed of sound (12), one can easily derive the dependence of these magnitudes on the density. The results for both functions are plotted in Fig. 11.

The spatial order of the solid is reflected in the shape

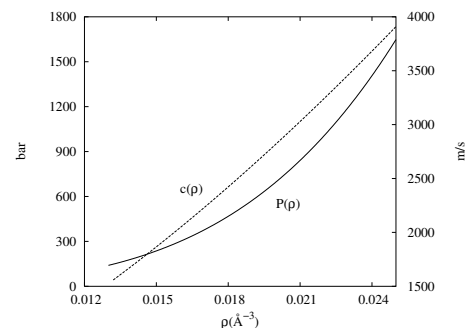


FIG. 11: Pressure and speed of sound of solid H \downarrow as a function of the density. Left (right) scale corresponds to pressure (speed of sound).

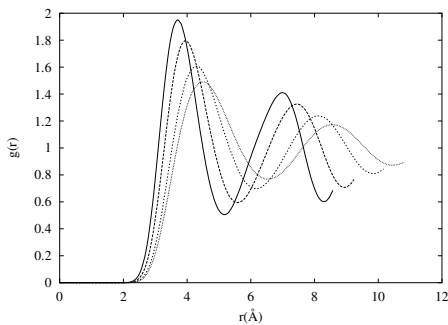


FIG. 12: Two-body radial distribution functions of the solid phase. From bottom to top in the height of the main peak, the results correspond to densities 0.0125, 0.015, 0.02, and 0.025 \AA^{-3} .

of the two-body radial distribution function $g(r)$. Results for $g(r)$ in the solid phase for different densities are shown in Fig. 12. At densities $\rho = 0.0125$ and 0.015\AA^{-3} , we can compare results for $g(r)$ in the gas and solid phases. As one can see, the peaks of the solid are slightly shifted to larger distances than in the gas and more importantly, and as expected, the secondary peaks of the solid are more pronounced. When ρ increases, the height of the peaks increases and moves to shorter distances, like in the gas phase.

D. Gas-solid phase transition

A relevant prediction that can be drawn from the present DMC results on the energies of the gas and solid phases of $\text{H}\downarrow$ is the location of the gas-solid phase transition. In order to determine the transition point and the corresponding freezing (ρ_f) and melting (ρ_m) densities, we have performed the Maxwell double-tangent construction as shown in Fig. 13. From the common tangent to both phases we obtain $\rho_f = 0.01328 \text{\AA}^{-3}$ and $\rho_m = 0.01379 \text{\AA}^{-3}$, which corresponds to a common pressure at the transition of $P = 173(15)$ bar. The melting pressure has proven to be quite independent of the lattice used in the simulation since using fcc and hcp we obtain 175 and 176 bar, respectively.

At the transition the kinetic energy per particle of the system is discontinuous. The size of this discontinuity in other quantum fluids such as He and Ne has received the interest in the past from both the theoretical and experimental sides.^{29,30,31} In the present system we are able to accurately measure this discontinuity: in the gas side at freezing $T/N = 44.0(5)$ K and in the solid side at melting $T/N = 51.5(6)$ K. Therefore, the discontinuity amounts to 7.5 K approximately. On the other hand, when the system crystallizes the condensate fraction of the gas is small but not zero, $n_0 = 0.04$.

The Lindemann's ratio, defined as $\gamma = \sqrt{\langle(\mathbf{r} - \mathbf{r}_I)^2\rangle}/a_L$, where a_L is the lattice constant, can also be obtained from the DMC simulations. At the

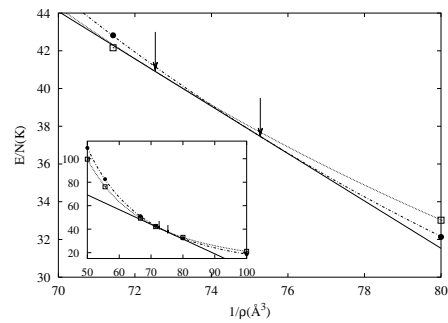


FIG. 13: Maxwell construction based on plotting the energy per particle, E/N as a function of $1/\rho$. The densities at which the first-order transition occurs are identified by finding the common tangent (solid line) to both the solid (dotted line) and gas curve (dot-dashed line). The inset shows the construction in a wider range of $1/\rho$.

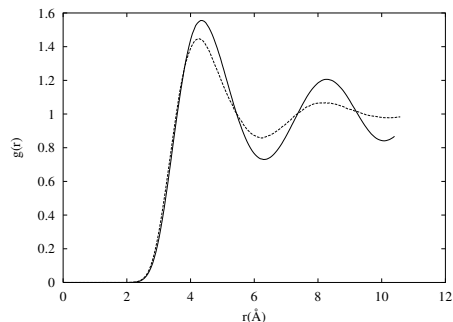


FIG. 14: Two-body radial distribution function at the gas-solid phase transition. The solid line corresponds to the solid at ρ_m and the dashed line to the gas at ρ_f .

melting point it is $\gamma = 0.25$, a nearly identical value to the one of solid ${}^4\text{He}$ ($\gamma = 0.26$).

The spatial structure of both phases at the transition point is rather different in spite of the small difference between ρ_f and ρ_m . In Fig. 14, we show results of $g(r)$ for both phases at the transition point. As one can see, the degree of localization is higher for the solid: the strength of the main peak is larger and the height of the subsequent peaks decreases more slowly than in the gas. Nevertheless, the signature of the solid phase manifests more clearly in $S(k)$. In Fig. 15, results of $S(k)$ for both phases are compared at densities ρ_f (gas) and ρ_m (solid). High intensity peaks located at the reciprocal lattice sites are a clear signature of the solid order; they are obviously absent in the $S(k)$ of the gas.

IV. CONCLUSIONS

The ground-state properties of spin-polarized hydrogen $\text{H}\downarrow$ have been accurately determined using the DMC method. The combination of the accuracy provided by the DMC and the precise knowledge of the $\text{H}\downarrow$ - $\text{H}\downarrow$ interatomic potential has allowed for a nearly exact determi-

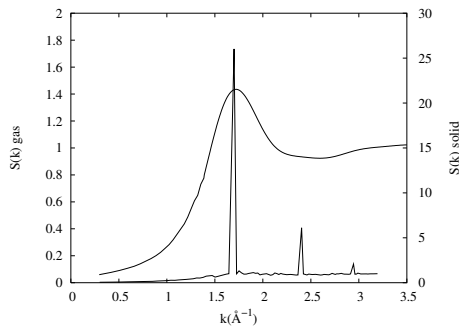


FIG. 15: Static structure factor at the gas-solid phase transition. The results correspond to the gas at ρ_f and to the solid at ρ_m .

nation of the main properties of the system, in both the gas and solid phases.

The light mass of the hydrogen atom and the shallow well of its interaction force $H\downarrow$ to remain a gas in the limit of zero temperature. In the very dilute limit, the equation of state of the gas is well described by the general expression of a weakly interacting Bose gas. This analytical behavior depends only on the gas parameter ρa^3 , with a the corresponding s-wave scattering length. Compared with other Bose-condensed gases, like the alkalis, hydrogen presents the appealing circumstance of the accurate knowledge we have of its interatomic interaction. This allows for the use of the real interaction in all the density regime, and thus accurate calculations at

much higher densities are possible.

When the density is high enough the systems freezes. We have studied the energetic and structural properties of the solid phase. Near melting the bcc phase is slightly preferred over the hcp and fcc ones. However, the energy differences between the lattices are very small and become indistinguishable at higher densities. From the DMC equations of state of the gas and solid phases, we have obtained the gas-solid transition point. At zero temperature, the transition occurs at $P = 173(15)$ bar. This value is significantly higher than previous estimations: 50 bar, obtained by using the quantum theory of corresponding states,¹ and 81 bar, from a VMC estimation by Danilowicz *et al.*¹⁹ It is worth noticing that the transition point depends dramatically on the accuracy of the theoretical method used for its calculation: if instead of using the DMC technique an estimation is performed using only the VMC method, one obtains $P = 113(17)$ bar, a value significantly smaller than the DMC result.

Acknowledgments

J. B. and J. C. acknowledge support from DGI (Spain) Grant No. FIS2005-04181 and Generalitat de Catalunya Grant No. 2005SGR-00779. We also acknowledge the support of the Central Computing Services at the Johannes Kepler University in Linz, where part of the computations was performed.

-
- ¹ W. C. Stwaley and L. H. Nosanow, Phys. Rev. Lett. **36**, 910 (1976).
² M. H. Anderson, J. R. Ensher, M. R. Matthews, C. E. Wieman, and E. A. Cornell, Science **269**, 198 (1995); K. B. Davis, M. O. Mewes, M. R. Andrews, N. J. van Druten, D. S. Durfee, D. M. Kurn, and W. Ketterle, Phys. Rev. Lett. **75**, 3969 (1995); C. C. Bradley, C. A. Sackett, J. J. Tollet, and R. G. Hulet, Phys. Rev. Lett. **75**, 1687 (1995).
³ D. G. Fried *et al.*, Phys. Rev. Lett. **81**, 3811 (1998).
⁴ A. I. Safonov, S. A. Vasilyev, I. S. Yasnikov, I. I. Lukashevich, and S. Jaakkola, Phys. Rev. Lett. **81**, 4545 (1998).
⁵ Z. Hadzibabic, P. Krueger, M. Cheneau, B. Battelier, and J. Dalibard, Nature **441**, 1118 (2006).
⁶ W. Kolos and L. Wolniewicz, J. Chem. Phys. **43**, 2429 (1965); Chem. Phys. Lett. **24**, 457 (1974).
⁷ M. J. Jamieson, A. Dalgarno, and L. Wolniewicz, Phys. Rev. A **61**, 042705 (2000).
⁸ M. D. Miller, L. H. Nosanow, Phys. Rev. B **15**, 4376 (1976).
⁹ R. D. Etters, J. V. Dugan, Jr., and R. W. Palmer, J. Chem. Phys. **62**, 313 (1975).
¹⁰ L. J. Lantto and R. M. Nieminen, J. Low. Temp. Phys. **37**, 1 (1979).
¹¹ P. Entel and J. Anlauf, Z. Phys. B **42**, 191 (1981).
¹² R. M. Panoff and J. W. Clark, Phys. Rev. B **36** 5527 (1987).
¹³ M. F. Flynn, J. W. Clark, E. Krotscheck, R. A. Smith, and R. M. Panoff, Phys. Rev. B **32**, 2945 (1985).
¹⁴ B. Skjetne and E. Østgaard, J. Phys.: Condens. Matter **11** 8017 (1999).
¹⁵ D. Blume, B. D. Esry, Chris H. Greene, N. N. Klausen, and G. J. Hanna, Phys. Rev. Lett. **89**, 163402 (2002).
¹⁶ N. N. Bogoliubov, J. Phys. (U.S.S.R.) **11**, 23 (1947).
¹⁷ T. D. Lee, K. Huang, and C. N. Yang, Phys. Rev. **106**, 1135 (1957).
¹⁸ T. T. Wu, Phys. Rev. **115**, 1390 (1959).
¹⁹ R. L. Danilowicz, J. V. Dugan, Jr., and R. D. Etters, J. Chem. Phys. **65**, 498 (1976).
²⁰ J. Boronat and J. Casulleras, Phys. Rev. B **49** 8920 (1994).
²¹ L. Vranješ, J. Boronat, J. Casulleras, and C. Cazorla, Phys. Rev. Lett. **95** 145302 (2005).
²² W. Kolos and J. Rychlewski, J. Mol. Spectrosc. **143**, 237 (1990).
²³ I. F. Silvera and V.V. Goldman, Phys. Rev. Lett. **45** 915 (1980).
²⁴ Zong-Chao Yan, James F. Babb, A. Dalgarno, and G. W. F. Drake, Phys. Rev. A **54**, 2824(1996).
²⁵ S. Giorgini, J. Boronat, and J. Casulleras, Phys. Rev. A **60**, 5129 (1999); J. Boronat, J. Casulleras, S. Giorgini, Physica B **284-288**, 1 (2000).
²⁶ Carl J. Williams, Paul S. Julienne, Phys. Rev. A **47** 1524 (1993).
²⁷ J. Casulleras and J. Boronat, Phys. Rev. B **52**, 3654 (1995).
²⁸ C. Pierleoni, D. M. Ceperley, and M. Holzmann, Phys. Rev. Lett. **93**, 146402 (2004).

²⁹ U. Bafle, M. Zoppi, F. Barocchi, R. Magli, and J. Mayers, Phys. Rev. Lett. **75**, 1957 (1995).

³⁰ D. M. Ceperley, R. O. Simmons, and R. C. Blasdel, Phys. Rev. Lett. **77**, 115 (1996).

³¹ M. Neumann and M. Zoppi, Phys. Rev. E **65**, 031203 (2002).